


RESEARCH ARTICLE

Evolution of errors in the global multiresolution model for prediction across scales: Shallow water (MPAS–SW)

Xiaoxu Tian 

Earth System Science Interdisciplinary
Center, University of Maryland,
Maryland, USA

Correspondence

X. Tian, Earth System Science
Interdisciplinary Center, University of
Maryland, MD, USA.
Email: xtian15@terpmail.umd.edu

Abstract

The global Model for Prediction Across Scales (MPAS) with shallow-water (SW) dynamics is taken as the forecast model to characterize the errors under a variable-resolution (VR) mesh. An idealized experiment featuring gravity and Rossby waves triggered by orography is conducted with two meshes consisting of the same number of grid cells, which directly indicates the computational cost. One mesh is of 120-km uniform resolution (UR), the other has 53–210 km VR. Both simulations are compared with the solutions from a 60-km uniform high-resolution (HR) mesh serving as the reference. The differences with respect to the HR results for both UR and VR experiments are manifested as rapidly propagating gravity waves circling the Earth about every two days. These signals are regarded as errors due to insufficient resolution. Over most of the Earth, the resolution of the VR mesh is coarser than that of the UR mesh. The magnitudes of the errors in the VR experiment are found to grow larger than those in the UR case shortly after the simulation starts. The sensitivities to the errors in the eight-day forecast calculated with the MPAS–SW adjoint model show similar propagation patterns, following a nonlinear state trajectory. The sensitivities under VR suggest that little contribution to the errors throughout the simulation process is made within the finely resolved areas. In the initial conditions under VR, the error signals come primarily from the coarse-resolution regions immediately outside the areas with enhanced resolution. This finding implies that, in simulations under VR, error signals generated in the coarsely resolved regions can be propagated into the finely resolved areas when conveyed by wave types allowed in the model, that is, gravity waves in the case of this study, the rate of which depends on the fluid mean height.

KEYWORDS

data assimilation, global model, solution errors, adjoint sensitivities, numerical methods, mesh size, variable resolution, shallow-water dynamics

1 | INTRODUCTION

The Model for Prediction Across Scales (MPAS) is a global modeling framework, under which geophysical dynamical cores such as atmospheric, oceanic, and shallow-water

(SW) can simulate and predict the evolution of fluids. One of the unique features of the MPAS is that it offers the option to perform global simulations at both uniform and smoothly variable resolutions (Ringler *et al.*, 2008; 2010; 2011; 2012; 2013). The model is spatially discretized

following the Arakawa C-grid with finite-volume irregular spherical centroidal Voronoi tessellation (SCVT) meshes (Thuburn *et al.*, 2009). In addition to globally uniform high resolution, under such an SCVT discretization scheme, regions of interest can be configured at high resolution while other areas throughout the globe may use relatively coarse resolution, with smooth transitions in between. The availability of such an option can serve as a rather economic solution to the age-old challenge of expensive computational costs in global numerical modeling (Satoh *et al.*, 2008). This capability to simulate under both uniform and variable resolution is applicable to both short-term weather and long-term climatological studies (Michaelis *et al.*, 2019). The smooth transition stands in contrast to abrupt resolution changes such as the nesting method in the Weather Research and Forecasting (WRF) model. A sudden change of resolution in the discretized grids is subject to generation of erroneous signals, which is not expected to be the case with smooth resolution transitions, as in MPAS. This advantage is confirmed in the study of Hagos *et al.* (2013). Several previous studies have explored the underlying issues of numerical simulations at variable resolution. The main conclusion of Ringler *et al.* (2011) is that solution error is controlled primarily by the grid resolution in the coarsest part of the model domain. Davies (2017) found that, in Limited-Area Model (LAM) simulations under both uniform and variable resolution, errors arise from the lower-resolution lateral boundary conditions and propagate into the regions of interest. In this study, it was also found that dynamical downscaling cannot recover the smaller scale features that are only resolvable at high resolution, which should have developed upstream of the lateral boundaries.

As introduced in Tian and Zou (2020) and Tian (2020), the tangent linear (TL) and adjoint (AD) models are critical additions to the nonlinear MPAS–Atmosphere and MPAS–SW dynamical cores, in their significant roles of diagnosing a variety of atmospheric model properties and forming variational data assimilation systems. Rabier *et al.* (1992) investigated the sensitivities of cyclogenesis to the model initial conditions using primitive atmospheric equations. Errico and Vukicevic (1992) demonstrated the sensitivities in two synoptic cases with the adjoint model of the Fourth Mesoscale Model (MM4) of Pennsylvania State University (PSU)–National Center for Atmospheric Research (NCAR). Errico (1997) discussed in detail the potential applicability of adjoint models to meteorological topics including sensitivity analysis, model singular vectors, and variational data assimilation. Zou *et al.* (1997) documented the development and application potential of the TL/AD version of the PSU–NCAR MM5 model and formulated a four-dimensional variational (4D-Var) assimilation system. In Tian and Zou (2020), the original

MPAS–Atmosphere dynamical core was restructured into a PYTHON–FORTRAN framework owing to the convenience offered by PYTHON. Under the same framework, the TL/AD version of MPAS–Atmosphere was developed, which demonstrated its applicability in efficient sensitivity analysis. In contrast to the nonhydrostatic dynamics simulated by MPAS–Atmosphere, MPAS–SW solves the SW equations numerically in a global domain; these equations are known for their simplicity and yet capability to simulate various atmospheric phenomena including gravity waves, barotropic instability, Rossby waves, and geostrophic adjustment (Holton, 1973). Tian (2020) documented the development of the MPAS–SW TL/AD, which was then applied to obtain the model’s singular vectors (SVs) to show the improved predictability under a smoothly variable-resolution mesh in the case of Hurricanes *Sandy* and *Joaquin*.

In this study, the nonlinear MPAS–SW model and its TL/AD models are applied in characterizing error evolution under meshes of both uniform and variable resolution. The sources of the errors will be analyzed quantitatively by showing the adjoint sensitivities of the the initial conditions to the error field at the final forecast time. In Section 2, the global MPAS shallow-water model is introduced briefly. Section 3 describes the development of TL/AD models for MPAS–SW and how to conduct sensitivity analysis with an adjoint model. In Section 4, the numerical results from both nonlinear forward and adjoint models will be analyzed. Section 5 summarizes and concludes this study.

2 | MPAS–SW MODEL AND TEST CASE DESCRIPTION

The shallow-water model is a widely employed tool in the field of meteorology. Among MPAS-related research, Ringler *et al.* (2008) formulated the shallow-water equations under SCVT meshes to test the validity of numerical simulations under discretization with SCVT. With the SW model, Ringler *et al.*, (2010,2011) tested the C-grid discretization under SCVT further with a set of standard idealized cases from Williamson *et al.* (1992) and verified that the numerical scheme in MPAS exhibits conservation of total energy within the time-truncation errors. In this study, the same SW model under the global MPAS framework and its TL/AD developed in Tian (2020) are adopted to demonstrate the error features under a variable-resolution SCVT mesh. The nonlinear continuous SW equations can be written as follows:

$$\frac{\partial h}{\partial t} + \nabla(\mathbf{h}\mathbf{u}) = 0, \quad (1)$$

$$\frac{\partial \mathbf{u}}{\partial t} + (\mathbf{u} \nabla) \mathbf{u} + f \mathbf{k} \times \mathbf{u} = -g \nabla (h + b), \quad (2)$$

in which the model prognostic variables include the fluid height h and wind component \mathbf{u} in directions normal to the cell edges; $f = 2\Omega \sin \theta$, where θ denotes latitude, and b are the Coriolis parameter and bottom topography heights, respectively. The time integral of Equations 1 and 2 is implemented following the fourth-order Runge–Kutta discretization scheme to achieve fourth-order accuracy in time (Ringler *et al.*, 2008), in which no limiter, filter, or dissipation is included. The MPAS–SW TL/AD models are built with the same temporal discretization. Spatially, the ∇^2 and ∇^4 dissipations are configurable in both the nonlinear forward and TL/AD models, in the presence of which small-scale energy will be dissipated with minimal impact on large-scale motions (Klemp, 2017). The initial conditions are specified following test case 5 (TC5) in Williamson *et al.* (1992), that is, zonal flow over an isolated mountain. The mountain heights are related to b in Equation 2 following the relationship

$$b_s = b_0(1 - r/R), \quad (3)$$

where $b_0 = 2000$ m, $R = 20^\circ$, and $r^2 = \min [R^2, (\lambda - \lambda_c)^2 + (\theta - \theta_c)^2]$. The center of the mountain is located at $[\lambda_c = 90^\circ\text{W}, \theta_c = 30^\circ\text{N}]$. The actual distribution of the mountain height from Equation 3 can be found as contoured in Figure 1. The wind field is derived from the streamfunction, which is initialized as

$$\psi = -a u_0 (\sin \theta \cos \alpha - \cos \lambda \cos \theta \sin \alpha), \quad (4)$$

where a is the radius of the Earth and $u_0 = 20$ m·s⁻¹, and α is the angle between the axis of solid-body rotation and the polar axis of the spherical coordinate system, which is 0 in the case of this study. The height field is then given as

$$gh = gh_0 - \left(a \Omega u_0 + \frac{u_0^2}{2} \right) \times (-\cos \lambda \cos \theta \sin \alpha + \sin \theta \cos \alpha)^2, \quad (5)$$

in which mean height $h_0 = 5960$ m and the rotation rate of the Earth $\Omega = 7.292 \times 10^{-5}$ rad·s⁻¹.

The mountain heights and wind field defined in Equations 3 and 4 are specified using three different meshes: (a) uniform 120-km resolution (UR) mesh with 40,962 grid cells in total, (b) mesh with variable resolution (VR) from 53–210 km, also consisting of 40,962 grid cells, and (c) uniform 60-km or high-resolution (HR) mesh having 163,842 grid cells. Under the condition of the same integration time-step size, the number of grid cells on a mesh directly indicates the computational cost of the simulations, as the MPAS model essentially loops over each cell to calculate the tendency terms following the dynamical

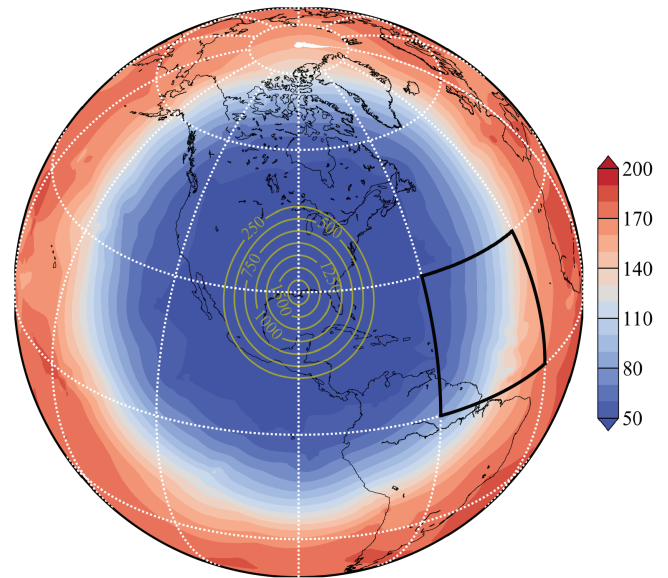


FIGURE 1 Average of cell-to-cell distance (shaded) in the variable-resolution mesh with 40,962 grid cells with the center of the refined resolution at $[30^\circ\text{N}, 90^\circ\text{W}]$, and the distribution of surface heights (contoured) in the idealized experiment [Colour figure can be viewed at wileyonlinelibrary.com]

relations. The shading in Figure 1 is the average cell-to-cell distance in the case of the VR mesh. The center of the area with refined resolution is at the same spot as the center of the mountain defined in Equation 3. Over the region marked by the black box in Figure 1, where the resolution gradually transitions, the spatial distributions of the hexagonal cells in the cases of UR, VR, and HR meshes are illustrated in Figure 2. The solutions of TC5 obtained under the HR mesh will serve as the referenced “truth” for simulations under the UR and VR meshes. The deviations from the HR solutions are regarded as errors due to insufficient resolution. As the zonal flow in the initial conditions (Figure 3a) passes over the mountain, Rossby waves are excited in the presence of nonlinear meridional variations of the Coriolis parameter serving as the restoring force, as well as gravity waves (Figure 3b–d).

3 | TL/AD OF MPAS–SW

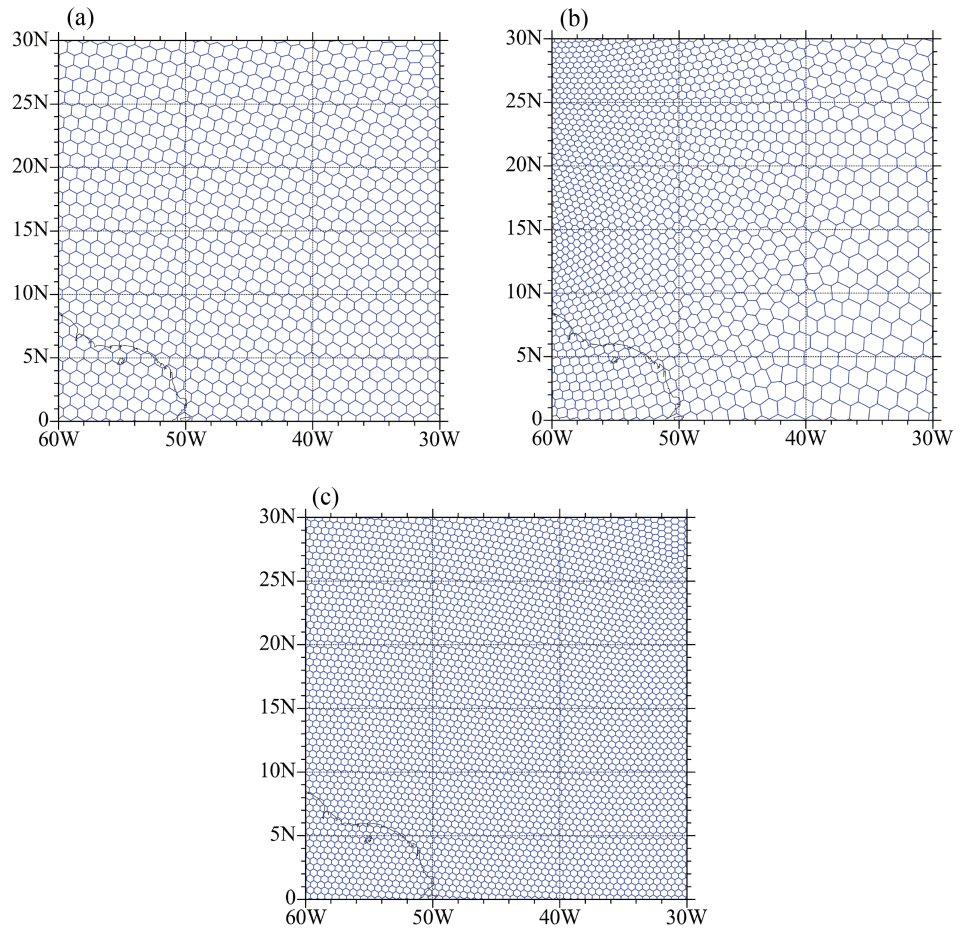
3.1 | Development of TL/AD

The nonlinear MPAS shallow-water dynamical core in Equations 1 and 2 can be expressed as

$$\mathbf{x}(t_r) = \mathcal{M}(\mathbf{x}(t_0)), \quad (6)$$

in which the model takes the initial condition $\mathbf{x}(t_0)$ (i.e., \mathbf{u} and h) at the starting time t_0 as input and solves SW

FIGURE 2 Spatial distributions of the hexagonal grid cells within the region defined with a black box in Figure 1, from (a) uniform 120-km resolution, (b) variable resolution, and (c) uniform 60-km resolution [Colour figure can be viewed at wileyonlinelibrary.com]



Equations 1 and 2 numerically to obtain the state variable $\mathbf{x}(t_r)$ at forecast time t_r . \mathcal{M} in this case is also called the nonlinear MPAS–SW forward operator. The tangent linear model of MPAS–SW can be developed following the relationship of Zou *et al.* (1997) and Tian (2020):

$$\Delta\mathbf{x}(t_r) = \mathbf{M}(\mathbf{x}(t_0))\Delta\mathbf{x}(t_0) = \frac{\partial\mathcal{M}(\mathbf{x}(t_0))}{\partial\mathbf{x}}\Delta\mathbf{x}(t_0), \quad (7)$$

where the symbol Δ denotes the perturbation of the nonlinear prognostic variable \mathbf{x} . The tangent linear operator \mathbf{M} is the derivative of \mathcal{M} with respect to every prognostic and diagnostic variable in the nonlinear MPAS–SW or the Jacobian of MPAS–SW. The TL model takes a small perturbation $\Delta\mathbf{x}(t_0)$ at time t_0 as input and predicts the perturbations $\Delta\mathbf{x}(t_r)$ at the forecast t_r evolved following the nonlinear state trajectory. The adjoint model \mathbf{M}^T is practically the transpose of the tangent linear model \mathbf{M} , which can be expressed as

$$\Delta\hat{\mathbf{x}}(t_0) = \mathbf{M}^T(\mathbf{x})\Delta\hat{\mathbf{x}}(t_r). \quad (8)$$

In Equation 7, the $\Delta\hat{\mathbf{x}}$ denote adjoint variables. The adjoint model integrates backwards from forecast time t_r to time t_0 . During the backward integration of the adjoint

model, nonlinear forward trajectories of the prognostic variables are required in the calculation process. Thus, in the practical implementation, the nonlinear forward model is first run to generate and store the prognostic variables at every time step from t_0 to t_r .

3.2 | Adjoint sensitivity analysis

The primary application of adjoint models is sensitivity analysis, which is the fundamental feature that derives other applications, including singular vectors and variational assimilation (Errico, 1997; Zou *et al.*, 1997). Tian and Zou (2020) demonstrated an example of adjoint sensitivity analysis with the MPAS–Atmosphere adjoint model in a baroclinic instability case. In the case of calculating sensitivities using an adjoint model, the quantity of interest (QOI, J) is first defined as

$$J = J(\mathbf{x}(t_r)), \quad (9)$$

in which J is a function of the model variable at the forecast time $\mathbf{x}(t_r)$. The QOI, also called the response function, can be a variety of variables: for example, mean squared

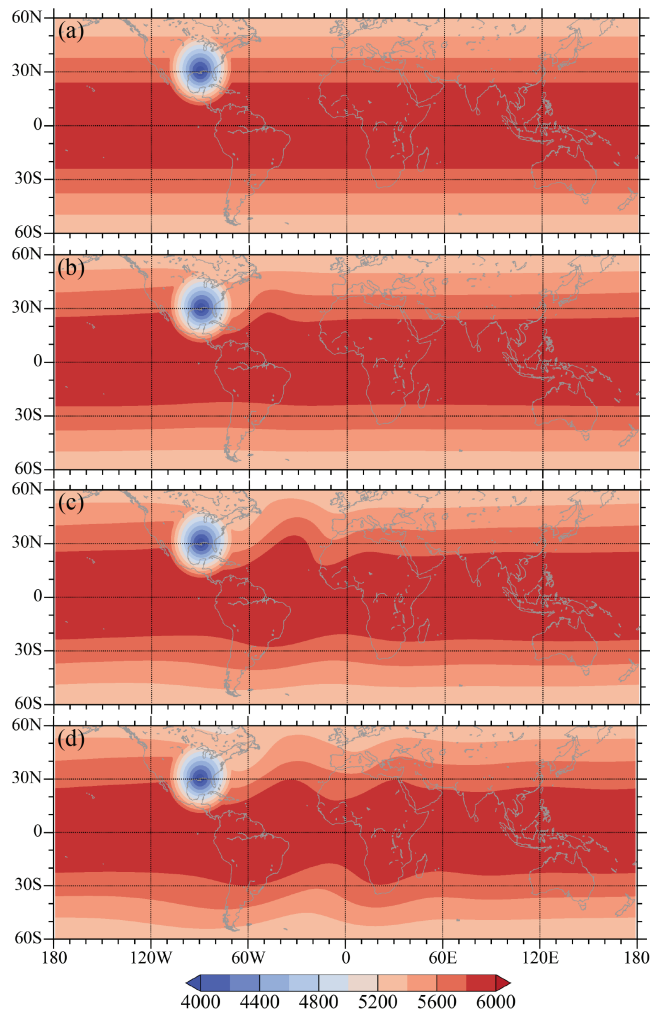


FIGURE 3 Spatial distribution of the height field of the high-resolution experiment in (a) the initial conditions and (b) two-day, (c) four-day, and (d) six-day forecasts simulated by the MPAS–SW model [Colour figure can be viewed at wileyonlinelibrary.com]

error (MSE), vorticity, surface pressure. Studies often aim to find the sensitivities of the response function at the forecast time to the state variables in the initial conditions. The approaches to finding such sensitivities generally involve comparing the outcomes of the model simulations with and without a slight perturbation in the initial conditions, that is, $J(\mathbf{x}(t_0) + \Delta\mathbf{x}(t_0))$ and $J(\mathbf{x}(t_0))$. Thus, the sensitivity of $J(\mathbf{x}(t_r))$ to the initial condition $\mathbf{x}(t_0)$ can be approximated by

$$\Delta J \approx \sum_k \frac{\partial J}{\partial x_{t_r,k}} \Delta x_{t_r,k}, \quad \Delta x_{t_r,k} \approx \sum_k \frac{\partial x_{t_r,j}}{\partial x_{0,k}} \Delta x_{0,k}. \quad (10)$$

In this approach, the magnitudes of the initial perturbations have to be small in order to obtain an accurate approximation of the gradient of J with respect to the perturbation $\Delta x_{0,k}$. In addition, the knowledge of the

sensitivity of J to all variables at all locations will require a great number of model runs. In comparison, finding the sensitivities of J with respect to the initial conditions with adjoint models can be expressed simply as (Errico, 1997)

$$\frac{\partial J}{\partial x_{0,j}} = \sum_k \frac{\partial x_{t_r,k}}{\partial x_{0,j}} \frac{\partial J}{\partial x_{t_r,k}}. \quad (11)$$

The term $\partial x_{t_r,k} / \partial x_{0,j}$ in Equation 11 is the transpose of the term $\partial x_{t_r,j} / \partial x_{0,k}$ in Equation 10, that is, the adjoint model. The sensitivities obtained following Equation 11 are accurate to the first order of approximation and independent of perturbation size. Also, the gradient of J with respect to all model variables at all spatial locations can be generated with only one adjoint model run. In this study, the response function will be the model error after an eight-day forecast, that is, $J = \frac{1}{2} \sum \Delta \mathbf{x}^2$. The MPAS–SW adjoint model will be used to quantify the sensitivity of the error after an eight-day forecast to the initial conditions.

4 | MODELING RESULTS

As introduced in Section 2, the solutions from the MPAS–SW for TC5 under uniform and variable-resolution meshes will be compared with the high-resolution experiment that serves as the “truth”, to characterize the errors. As the solutions from each experiment are inherently of different resolution and are located at different spatial locations, they are first interpolated onto a $1^\circ \times 1^\circ$ rectangular gridded map for convenience of comparison. Figure 4 shows the differences between the solutions under the UR mesh and those under the HR mesh after 0 (t_0), 12, 24, 36, and 48 hr. At the initial time, no significant features can be found except within the mountain region. After a 12-hr forecast, evident wave patterns start to radiate from the mountain area throughout the globe and reach the opposite site of the sphere at a time of 24 hr. The waves keep propagating around the globe and reach the region slightly to the east of the mountain at a time of 48 hr. Similarly, the differences in the solutions between the VR and HR meshes are given in Figure 5. The patterns and the propagation speed are the same as those in the UR case in Figure 4. However, the magnitudes of the waves in Figure 5 are visibly greater than those in Figure 4, especially in the results after 36 hr. As illustrated in Figure 1, the resolution is about 210 km outside the region with fine resolution, which is coarser than the uniform 120-km mesh. Thus, when the wave patterns are propagating at coarse resolution, the magnitude of the errors becomes increasingly greater and will return to the area with enhanced resolution, as shown in Figure 5e. To demonstrate the wave features for a longer time-scale, the Hovmöller diagrams of

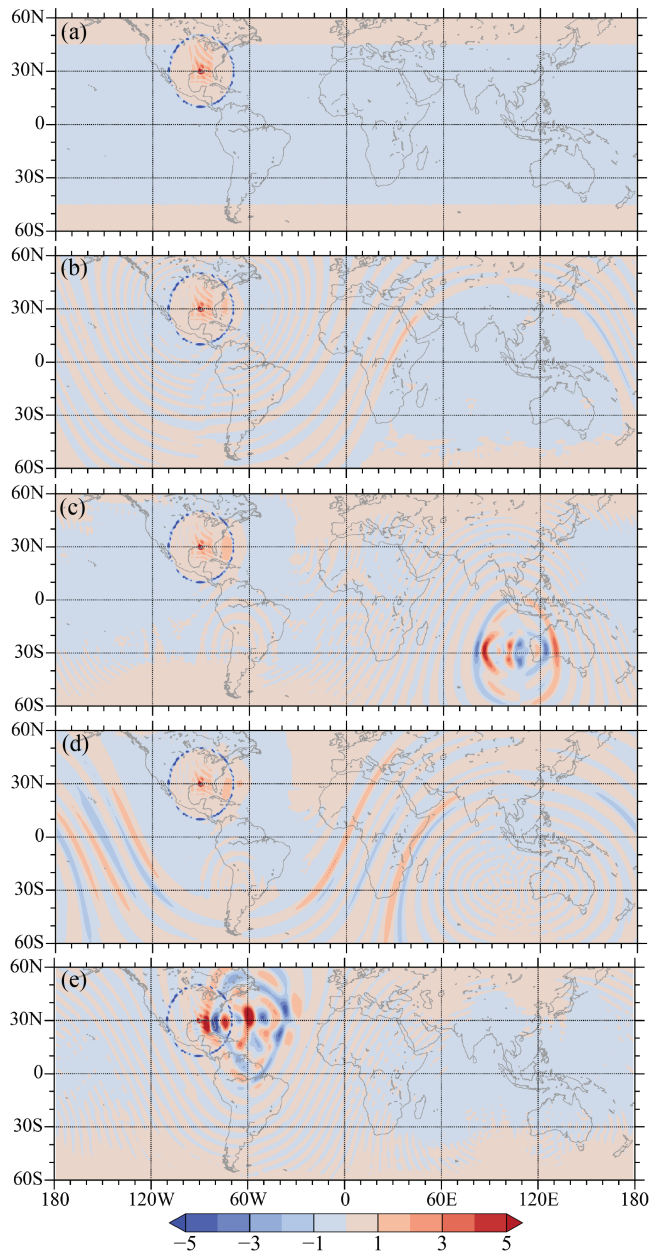


FIGURE 4 Differences in the simulated height field between the UR and uniform high-resolution reference experiments after (a) 0, (b) 12, (c) 24, (d) 36, and (e) 48 hr [Colour figure can be viewed at wileyonlinelibrary.com]

the errors at the Equator from the initial time to a forecast time of 8 days are given in Figure 6. Given the mean height of 5,960 m, the phase speed of the gravity waves is expected to be about $c_g = \sqrt{gh_0} = 241.8 \text{ m}\cdot\text{s}^{-1}$. These waves take 1.918 days to circle the Earth with a circumference of $2\pi a = 4.007 \times 10^7 \text{ m}$. Similarly to Figures 4 and 5, the wave patterns circle the Earth about every two days, while the pattern shifts slowly eastward following the Rossby waves excited due to the orography. The magnitudes of the signals constantly grow bigger in both UR and VR cases as they

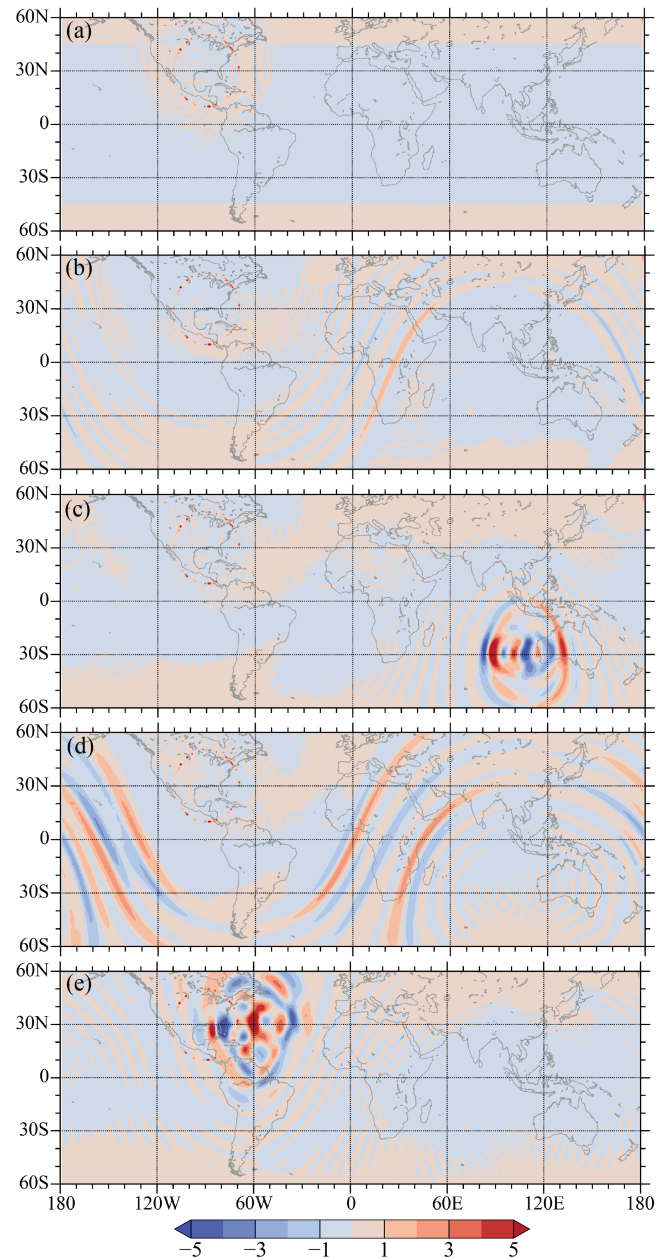


FIGURE 5 Differences in the simulated height field between the VR and uniform high-resolution reference experiments after (a) 0, (b) 12, (c) 24, (d) 36, and (e) 48 hr [Colour figure can be viewed at wileyonlinelibrary.com]

propagate, with those at VR growing significantly faster than those at UR.

To trace the sources of these gravity-wave error patterns quantitatively, the adjoint model of the MPAS-SW is sought hereafter. The response function J introduced in Section 3.2 in this case is defined as the total squared error after an eight-day forecast, the spatial patterns of which for both UR and VR experiments are shown in Figure 7. As observed in Figure 6, the magnitudes of the error signals are remarkably greater in the VR case than in the UR case.

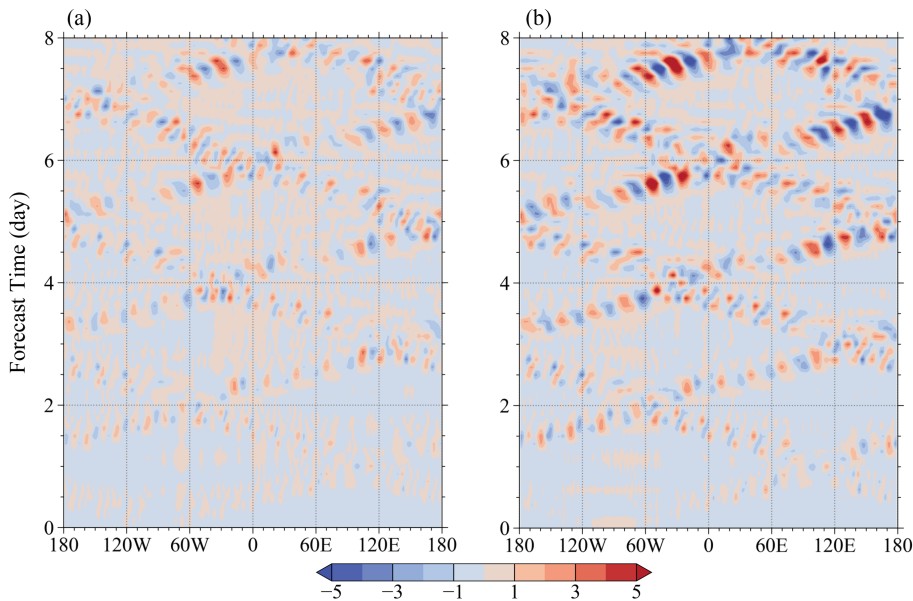


FIGURE 6 Differences between (a) the UR experiment and the high-resolution experiment and (b) the VR experiment and the HR experiment at the Equator (x -axis) with respect to the forecast time (y -axis) [Colour figure can be viewed at wileyonlinelibrary.com]

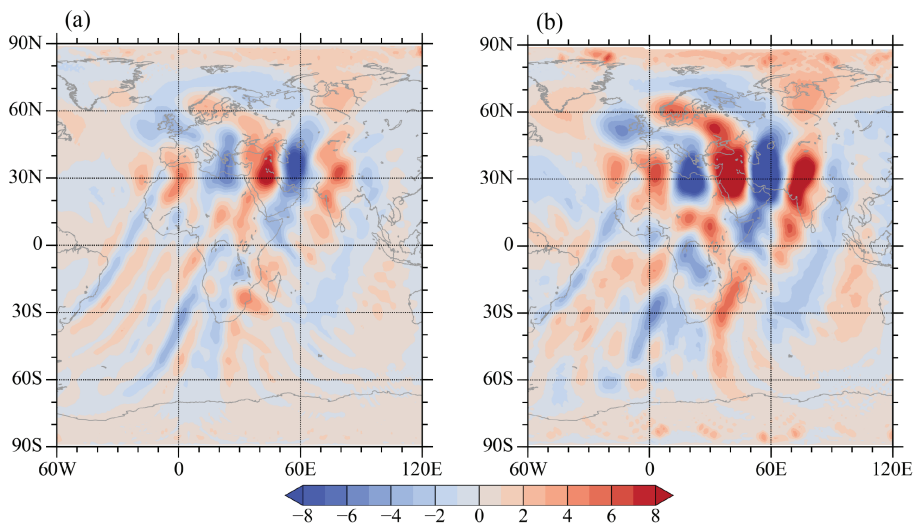


FIGURE 7 Differences in the simulated height field (a) between the UR and the uniform high-resolution reference experiments and (b) between the VR and the uniform high-resolution reference experiments after eight days [Colour figure can be viewed at wileyonlinelibrary.com]

These patterns are then taken by the adjoint model as the input at the time $t_r = 8$ days and are integrated backward in time to the initial time $t_0 = 0$. Figures 8 and 9 show the evolution of the sensitivities generated by the MPAS–SW adjoint model starting from 8 days and backward in time in the cases of the UR and VR experiments, respectively. Similarly to the forward propagation of the error signals, the sensitivities also evolve like gravity waves circling the Earth. Only several time moments where the sensitivity patterns pass through the area with refined resolution are selected for display in Figures 8 and 9. In the case of UR (Figure 8), the patterns travel through the region without “interruptions”. In comparison, whenever the signal travels to areas where the resolution is enhanced (as contoured in Figure 9), the sensitivity becomes close to zero, indicating the insensitivity of forecast errors to the dynamics

taking place within the area. When the adjoint model is integrated to the time t_0 , sensitivities are found primarily within the area where the mountain is configured. In the case under the VR mesh, all sensitive regions are found outside areas with refined resolution. Similarly to Figure 6, the Hovmöller diagrams of the adjoint sensitivities following the adjoint calculations are shown in Figure 10. We remind the reader that the adjoint model started calculation at the end of day 8 from the initial time, as is also indicated by the inverted y -axis. Agreeing with the findings in Figure 6, the sensitivities circle the Earth about every two days and propagate slowly westward following the Rossby waves in a nonlinear trajectory. The magnitudes of the adjoint sensitivities are found to remain consistent, within the fluctuations, with respect to the integration time, implying consistent contributions to the errors

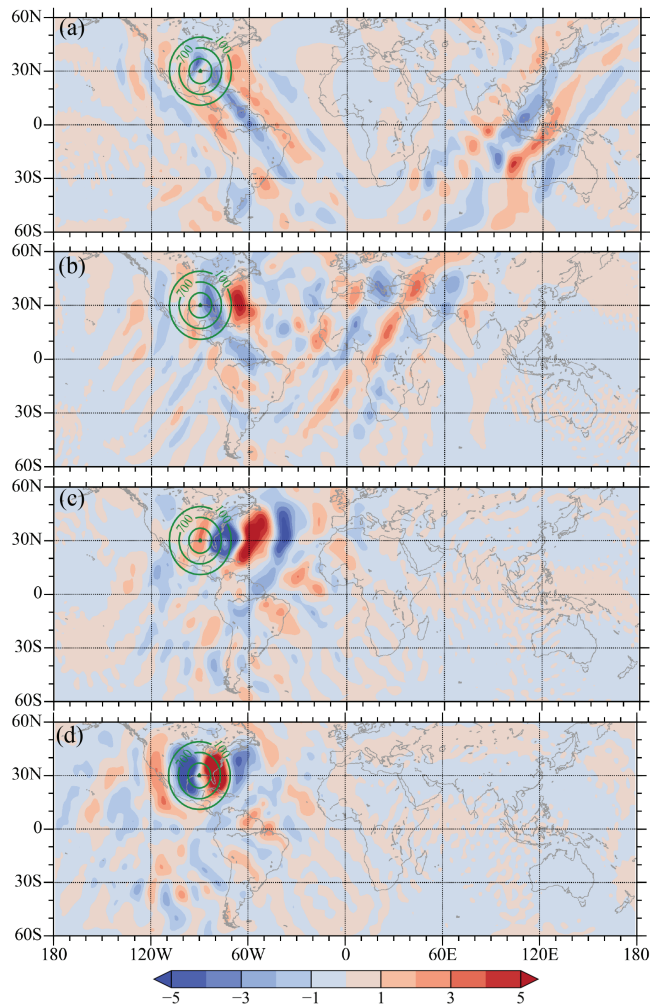


FIGURE 8 The adjoint sensitivities to the model resolution errors in the height field, (a) 36, (b) 102, (c) 144, and (d) 192 hr prior to the day 8 forecast in the UR experiment. The mountain heights are indicated by the green contoured curves [Colour figure can be viewed at wileyonlinelibrary.com]

shown in Figure 7 along the path of error propagation. In the case of the VR experiment (Figure 10b), however, the absolute values of the sensitivities decrease rapidly as the signal propagates near the region with enhanced resolution, which agrees with the demonstration in Figure 9. In addition, unlike those in Figure 6, the paths and the magnitudes of the sensitivities are strictly linear in Figure 10, as the adjoint model is essentially the transpose of the linearized MPAS-SW model, which is subject to the accuracy offered by a linear approximation. Throughout the adjoint calculation, no sensitivities can be found near the longitudinal region with enhanced resolution (indicated by the black dashed line in Figure 10b), as the dynamical equations are solved with sufficient resolution at those geographical locations, whereas large sensitivity values in coarsely resolved areas indicate that all errors come from the peripheries.

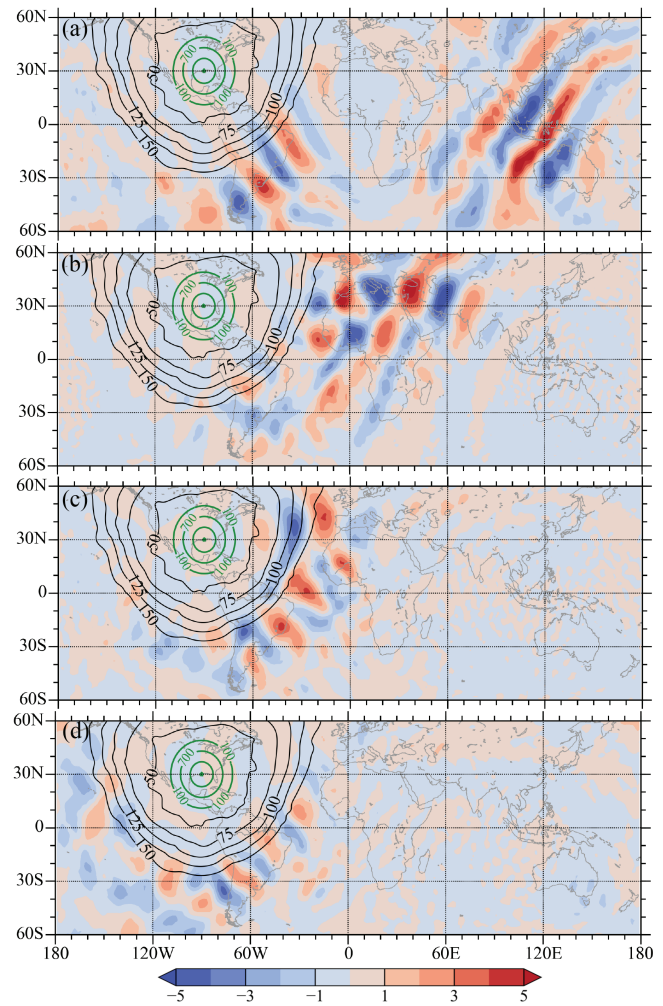


FIGURE 9 The adjoint sensitivities in the height field, (a) 36, (b) 102, (c) 144, and (d) 192 hr prior to the day 8 forecast in the VR experiment. The average of the cell-to-cell distances that were color-shaded in Figure 1 are indicated by the black contoured curves, and mountain heights by the green curves [Colour figure can be viewed at wileyonlinelibrary.com]

5 | SUMMARY AND CONCLUSIONS

The idealized simulation experiment of zonal flow over an orographic region in Williamson *et al.* (1992), which triggers both gravity and Rossby waves, is conducted under SCVT meshes of uniform 120-km resolution (UR), variable resolution (VR) from 53–210 km, and uniform 60-km high resolution (HR). The UR and VR meshes consist of exactly the same number of grid cells, indicating the same computational cost. The purpose is to explore, with the same amount of resources spent, how the VR mesh is likely to perform in simulating in the emphasized region with enhanced resolution as opposed to solutions with uniform resolution. In quantifying the answer to this question, the HR solutions are treated as references to be compared with the simulations under both UR and VR meshes, in

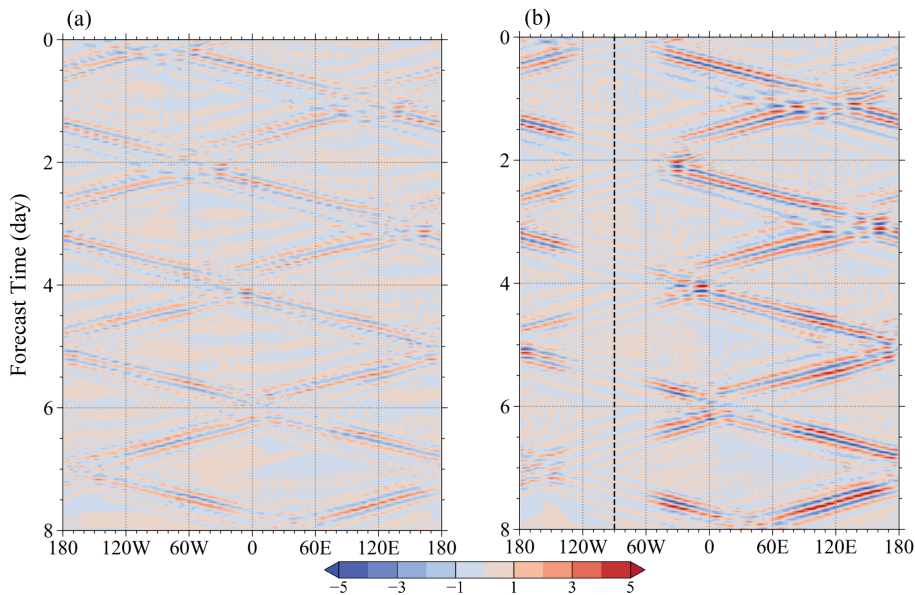


FIGURE 10 The adjoint sensitivities to the model resolution errors in the height field at the Equator (x-axis) with respect to the forecast time (y-axis, backward), for (a) the UR experiment and (b) the VR experiment. The center longitude of the refined resolution in the VR mesh is indicated by the dashed line in (b) [Colour figure can be viewed at wileyonlinelibrary.com]

order to characterize the fraction of errors in the solution due to insufficient resolution. The differences in solution for UR or VR compared with HR show error signals as rapidly propagating gravity waves, which can circle the Earth within two days. In addition to the fast propagation, the magnitude of the errors is constantly growing in both UR and VR cases. As the resolution over the majority of the Earth is coarser in the VR mesh than in the UR mesh, the magnitude growth of errors under VR is significantly faster than under UR. In addition, the constantly growing errors can propagate back to the area of interest about every two days.

Taking the errors in the eight-day forecasts as the response function, the MPAS-SW adjoint model developed in Tian (2020) was employed in this study to obtain the sensitivities to the forecast errors at earlier times including initial conditions. Following the nonlinear state trajectories, the sensitivities calculated with the adjoint model show propagation similar to the error gravity waves found in the nonlinear forward solutions. The main difference in the spatial distribution of the sensitivities between UR and VR cases is that small sensitivities can be found within areas of refined resolution in the VR experiment, suggesting minimal contribution to the errors comes from solving dynamical equations within that region. The adjoint sensitivities in the initial conditions demonstrate that, in the UR experiment, the errors are primarily from the areas where the mountain is located, whereas in the VR experiment the sensitivities are located mainly at coarse resolution immediately outside the refined area. The findings show that, even though, within the area of interest, the dynamical equations are solved at high resolution, the solutions are still subject to errors or deficiencies generated

elsewhere, which propagate into the finely resolved area.

ACKNOWLEDGEMENTS

The author thanks NCAR for releasing the MPAS shallow-water model for public access. The author is grateful for the anonymous reviewers whose comments and suggestions helped improve and clarify this article. The modeling results for producing the figures in this study are available at <http://www.xiaoxutian.com/products/>.

ORCID

Xiaoxu Tian  <https://orcid.org/0000-0002-2832-4790>

REFERENCES

- Davies, T. (2017) Dynamical downscaling and variable resolution in limited-area models. *Quarterly Journal of the Royal Meteorological Society*, 143(702), 209–222.
- Errico, R.M. (1997) What is an adjoint model? *Bulletin of the American Meteorological Society*, 78(11), 2577–2592.
- Errico, R.M. and Vukicevic, T. (1992) Sensitivity analysis using an adjoint of the PSU-NCAR mesoseale model. *Monthly Weather Review*, 120(8), 1644–1660.
- Hagos, S., Leung, R., Rauscher, S.A. and Ringler, T. (2013) Error characteristics of two grid refinement approaches in aquaplanet simulations: MPAS-A and WRF. *Monthly Weather Review*, 141(9), 3022–3036.
- Holton, J.R. (1973) An introduction to dynamic meteorology. *American Journal of Physics*, 41(5), 752–754.
- Klemp, J.B. (2017) Damping characteristics of horizontal Laplacian diffusion filters. *Monthly Weather Review*, 145(11), 4365–4379.
- Michaelis, A.C., Lackmann, G.M. and Robinson, W.A. (2019) Evaluation of a unique approach to high-resolution climate modeling using the model for prediction across scales-atmosphere (MPAS-A) version 5.1. *Geoscientific Model Development*, 12(8), 3725–3743.

- Park, S.-H., Skamarock, W.C., Klemp, J.B., Fowler, L.D. and Duda, M.G. (2013) Evaluation of global atmospheric solvers using extensions of the Jablonowski and Williamson baroclinic wave test case. *Monthly Weather Review*, 141(9), 3116–3129.
- Rabier, F., Courtier, P. and Talagrand, O. (1992) An application of adjoint models to sensitivity analysis. *Beiträge zur Physik der Atmosphäre*, 65(3), 177–192.
- Ringler, T., Ju, L. and Gunzburger, M. (2008) A multiresolution method for climate system modeling: application of spherical centroidal Voronoi tessellations. *Ocean Dynamics*, 58(5–6), 475–498.
- Ringler, T.D., Thuburn, J., Klemp, J.B. and Skamarock, W.C. (2010) A unified approach to energy conservation and potential vorticity dynamics for arbitrarily-structured c-grids. *Journal of Computational Physics*, 229(9), 3065–3090.
- Ringler, T.D., Jacobsen, D., Gunzburger, M., Ju, L., Duda, M. and Skamarock, W. (2011) Exploring a multiresolution modeling approach within the shallow-water equations. *Monthly Weather Review*, 139(11), 3348–3368.
- Satoh, M., Matsuno, T., Tomita, H., Miura, H., Nasuno, T. and Iga, S.-I. (2008) Nonhydrostatic icosahedral atmospheric model (NICAM) for global cloud resolving simulations. *Journal of Computational Physics*, 227(7), 3486–3514.
- Skamarock, W.C., Klemp, J.B., Duda, M.G., Fowler, L.D., Park, S.-H. and Ringler, T.D. (2012) A multiscale nonhydrostatic atmospheric model using centroidal Voronoi tessellations and c-grid staggering. *Monthly Weather Review*, 140(9), 3090–3105. <https://doi.org/10.1175/MWR-D-11-00215.1>.
- Thuburn, J., Ringler, T.D., Skamarock, W.C. and Klemp, J.B. (2009) Numerical representation of geostrophic modes on arbitrarily structured c-grids. *Journal of Computational Physics*, 228(22), 8321–8335.
- Tian, X. (2020) Predictability analysis with singular vectors of the multiresolution global shallow-water model. *Journal of the Atmospheric Sciences*. Under review.
- Tian, X. and Zou, X. (2020) Development of the tangent linear and adjoint models of the MPAS–Atmosphere dynamic core and applications in adjoint relative sensitivity studies. *Tellus*. 72(1), 1–17.
- Williamson, D.L., Drake, J.B., Hack, J.J., Jakob, R. and Swarztrauber, P.N. (1992) A standard test set for numerical approximations to the shallow-water equations in spherical geometry. *Journal of Computational Physics*, 102(1), 211–224.
- Zou, X., Vandenberghe, F., Pondevca, M. and Kuo, Y.-H. (1997). Introduction to adjoint techniques and the MM5 adjoint modeling system. NCAR Technical Note, NCAR, Boulder, Colorado.

How to cite this article: Tian X. Evolution of errors in the global multiresolution model for prediction across scales: Shallow water (MPAS–SW). *QJR Meteorol Soc.* 2020;1–10. <https://doi.org/10.1002/qj.3923>